



Structural, physical, and magnetic properties of nanocrystalline manganese-substituted lithium ferrite synthesized by sol–gel autocombustion technique

W. R. Agami¹ · M. A. Ashmawy²

Received: 13 April 2020 / Accepted: 18 June 2020 / Published online: 26 June 2020
© Springer-Verlag GmbH Germany, part of Springer Nature 2020

Abstract

Nanoparticles of spinel ferrite $\text{Li}_{0.5-0.5x}\text{Mn}_x\text{Fe}_{2.5-0.5x}\text{O}_4$ ($x=0, 0.25, 0.5, 0.75$ and 1) were prepared by sol–gel autocombustion technique. The crystalline phase formation, morphology, cation distribution, and magnetic properties of $\text{Li}_{0.5-0.5x}\text{Mn}_x\text{Fe}_{2.5-0.5x}\text{O}_4$ nanoferrite samples were investigated by X-ray diffraction (XRD), transmission electron microscopy (TEM), infrared (IR) spectroscopy, and vibrating sample magnetometer (VSM). The lattice parameter increases by Mn substitution, while both the crystallite size and Curie temperature (T_C) decrease. Values for both the saturation magnetization (M_s) and the coercivity (H_C) were enhanced because both are larger for Mn-substituted samples than those for unsubstituted ones. The addition of Mn^{2+} ions promotes (M_s) until ($x=0.5$) then an appreciable decrease occurs, whereas the coercivity (H_C) increases up to $x=0.25$ then it decreases. The role of the substitution with Mn^{2+} ions in changing all investigated properties of lithium ferrite was explained according to different theories.

Keywords Li–Mn nanoferrite · Sol–gel autocombustion · IR spectroscopy · XRD · Magnetic properties

1 Introduction

Lithium ferrite and substituted lithium ferrites have important and interesting technological applications, such as cathode materials in lithium-ion batteries [1–3]. They are commonly used in microwave applications and cores of high frequency inductors. The reason is that they have high (T_C), good thermal stability, excellent hysteresis squareness, and economical price [4, 5]. In the past, the solid-state reaction method was used to produce these materials. This method has many disadvantages, like chemical inhomogeneity, coarser crystallite size, and introduction of impurities during ball milling [6–8]. Recently, co-precipitation, hydrothermal, and sol–gel preparation techniques have been developed [9–12]. More attention has been focused toward the citrate–nitrate precursor autocombustion method

which permits preparing ultra-fine powders with chemically homogeneous composition, uniform size, and good reactivity [13, 14]. In fact, some authors investigated Mn-substituted lithium ferrite with composition ($\text{Li}_{0.5}\text{Mn}_x\text{Fe}_{2.5-x}\text{O}_4$) (where Mn enters the chemical formula on the expense of Fe only) [15–21]. The effect of sintering temperature (1080, 1032, and 984 °C) on the structural, electrical, and magnetic properties of autocombustion prepared sample of composition $\text{Li}_{0.45}\text{Mn}_{0.1}\text{Fe}_{2.45}\text{O}_4$ was carried out [22]. The structural and dielectric properties of $\text{Li}_{0.5}\text{Fe}_{2.5-0.5x}\text{Co}_x\text{Mn}_x\text{O}_4$ ($x=0.0$ – 0.5) fabricated by micro-emulsion method were studied [23]. Moreover, the structural and magnetic properties of $\text{Li}_{0.5-0.5x}\text{Mn}_x\text{Fe}_{2.5-0.5x}\text{O}_4$ (where $x=0$ to 1) prepared by the standard ceramic technique, i.e., microsize samples, have been reported [24]. However, according to the literature survey, there are no studies concerned with substitutions with Mn^{2+} ions on the expense of both Li^{1+} and Fe^{3+} ions according to the chemical formula ($\text{Li}_{0.5-0.5x}\text{Mn}_x\text{Fe}_{2.5-0.5x}\text{O}_4$) to prepare nanoparticles by sol–gel autocombustion method which is a low-temperature technique. Therefore, this present work aims at preparing, characterizing, and improving the magnetic properties of the Li ferrite by further Mn substitution of ($\text{Li}_{0.5-0.5x}\text{Mn}_x\text{Fe}_{2.5-0.5x}\text{O}_4$) system.

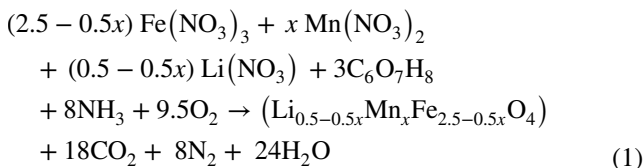
✉ W. R. Agami
Walid_abdelrasheed@sci.asu.edu.eg

¹ Physics Department, Faculty of Science, Ain Shams University, 11566 Abbassia, Cairo, Egypt

² Basic Science Department, Modern Academy for Engineering and Technology, El Mokattam, Cairo, Egypt

2 Experimental

Spinel ferrites of chemical formula $\text{Li}_{0.5-0.5x}\text{Mn}_x\text{Fe}_{2.5-0.5x}\text{O}_4$ ($x=0, 0.25, 0.5, 0.75, \text{ and } 1$) were prepared by sol–gel autocombustion method. Analytical grade of $(\text{LiNO}_3, \text{anhydrous})$, $(\text{Mn}(\text{NO}_3)_2 \cdot 4\text{H}_2\text{O})$, and $(\text{Fe}(\text{NO}_3)_3 \cdot 9\text{H}_2\text{O})$ have been weighed due to their stoichiometric proportions. They were dissolved in deionized water with subsequent addition of citric acid. The ratio of citric acid to total metal nitrates was 1:1. Ammonia was then added until the pH of the solution reached 8.3. Figure 1 shows the flow chart of the detailed processes of sol–gel autocombustion method. The chemical reaction of sol–gel autocombustion process is supposed to be as follows:



The produced gases were determined according to Reference [25].

X-ray diffraction (XRD) patterns of all samples were got at room temperature on Philips X^{PERT} Graphics and identified using Cu-K_α radiation. Indexing has been done using JCPDS (Joint Committee on Powder Diffraction Standard) cards of the ordered $\text{Li}_{0.5}\text{Fe}_{2.5}\text{O}_4$ (no. 75-0407) and MnFe_2O_4 (no. 74-2403). The lattice parameter (a) values were calculated from the following relation:

$$a = d_{hkl} (h^2 + k^2 + l^2)^{1/2} \quad (2)$$

To get more accuracy, these values of lattice parameters for each reflected plane were plotted against the function

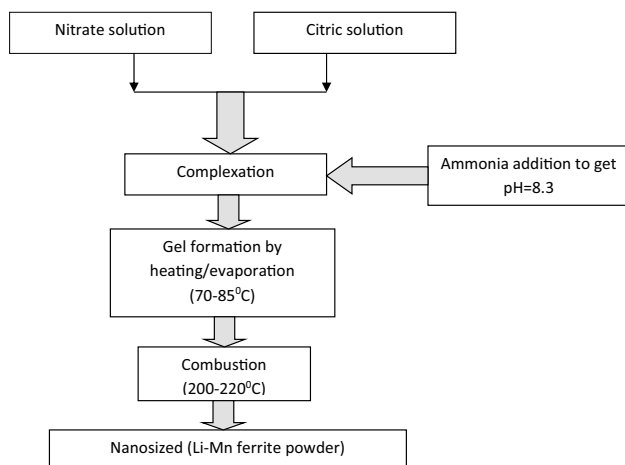


Fig. 1 Flow chart of sol–gel autocombustion process

$F(\theta) = \frac{1}{2} \left[\frac{\cos^2 \theta}{\sin \theta} + \frac{\cos^2 \theta}{\theta} \right]$, where θ is Bragg's angle, where straight lines were obtained. The accurate values of (a) were determined from extrapolation of these lines to $F(\theta) = 0$ [26]. Information on the microstructure (crystallite size (D) and microstrain (ϵ)) were revealed by performing individual peak fitting for the following planes: (220), (311), (400), (422), (511), and (440). The values of full width at half maximum (β) were obtained for each peak. Then, Williamson–Hall plots were drawn to get average values of the microstrain and crystallite size using the following formula [12, 27, 28]:

$$\beta \cos \theta = \frac{0.9\lambda}{D} + 4\epsilon \sin \theta \quad (3)$$

where λ is the X-ray wavelength ($\lambda = 1.54056 \text{ \AA}$).

The theoretical X-ray density (d_x) of all samples was calculated according to the formula ($d_x = \frac{8m}{Na^3}$), where m is the molecular mass and N is Avogadro's number. The practical density (d) of each sample was measured in double-distilled water using Archimedes' principle. The porosity percentage ($P\%$) was calculated from the following formula:

$$P = 100 \left(1 - \frac{d}{d_x} \right). \quad (4)$$

Transmission electron microscope (TEM, JEOL JEM-100CX) with accelerating voltage up to 100 kV was used to investigate the powder morphology. The average particle size was estimated from TEM images.

PERKIN ELMER 1430 Ratio Recording IR spectrophotometer was used to record the IR transmission spectra of all samples of $(\text{Li}_{0.5-0.5x}\text{Mn}_x\text{Fe}_{2.5-0.5x}\text{O}_4)$ in the wavenumber range 200–1000 cm^{-1} .

Vibrating sample magnetometer (VSM, EG&G PARC model no.1551 USA) was used to measure the magnetization of the powder samples. The magnetocrystalline anisotropy constant k_1 was obtained from Brown's relation [29]:

$$H_c = \frac{2k_1}{M_s},$$

where H_c is the coercivity determined from the hysteresis loop. Toroidal samples were used as transformer cores to determine the Curie temperature T_C according to a formerly demonstrated manner [30].

3 Results and discussion

3.1 XRD analysis

XRD patterns of $\text{Li}_{0.5-0.5x}\text{Mn}_x\text{Fe}_{2.5-0.5x}\text{O}_4$ nanoferrite samples are shown in Fig. 2. The peaks show a single-phase spinel ferrite structure. In fact, this is a clue that Mn^{2+} ions

substitute not only Fe^{3+} ions but also Li^{1+} ions because if this is not the situation, the quantities of Li^{1+} ions and Fe^{3+} ions would be less and more, respectively, than required for the phase $\text{Li}_{0.5}\text{Mn}_x\text{Fe}_{2.5-x}\text{O}_4$ to compose. This case must lead to other detected phases which are not found in these diffractograms. Moreover, all reflections are observed to shift to lower values, which implies an increase in the lattice parameter due to Mn doping (confirmed in Fig. 3). Such an increase in the lattice parameter is consistent with the difference in ionic radii, where the ionic radius of Mn^{2+} ion is larger than the average ionic radii of Fe^{3+} and Li^{1+} (the ionic

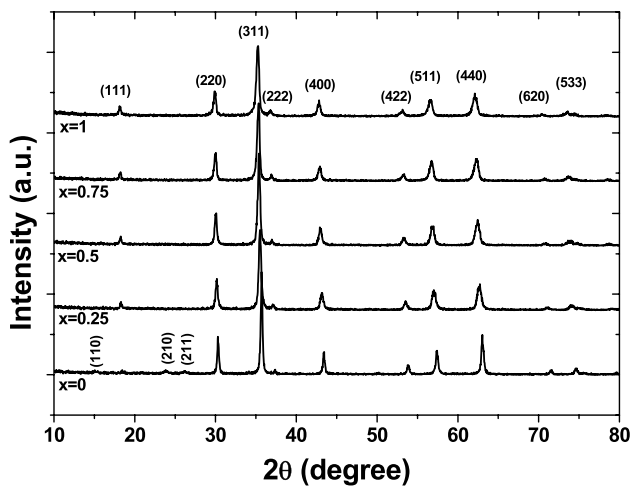
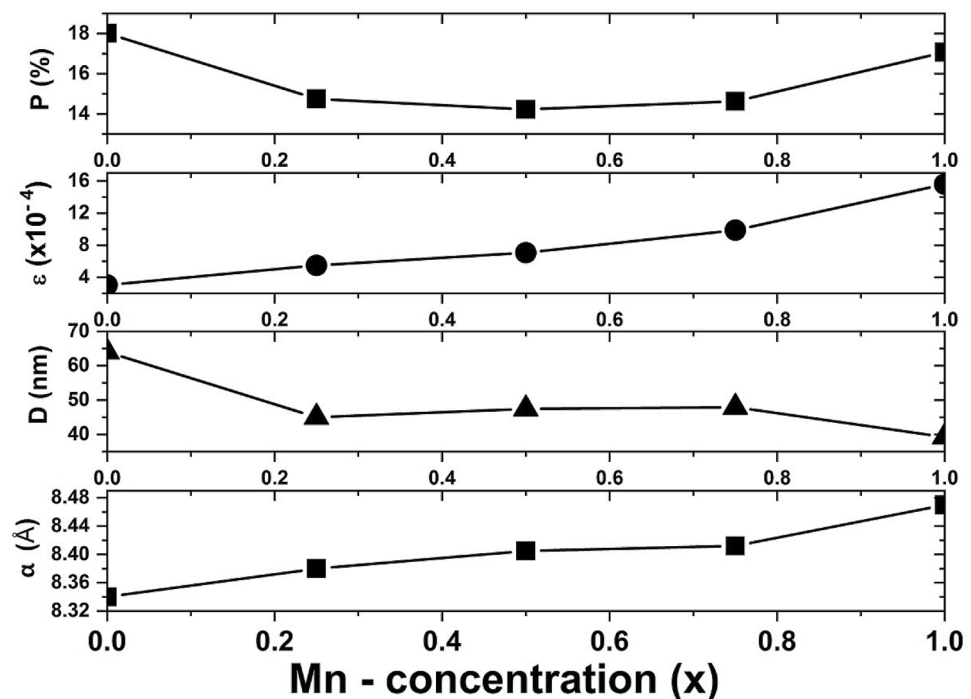


Fig. 2 X-ray diffraction patterns for $\text{Li}_{0.5-0.5x}\text{Mn}_x\text{Fe}_{2.5-0.5x}\text{O}_4$ ($x=0, 0.25, 0.5, 0.75,$ and 1) nanoferrite samples

Fig. 3 Lattice parameter (a), crystallite size (D), micro-strain (ϵ), and porosity (P) for $\text{Li}_{0.5-0.5x}\text{Mn}_x\text{Fe}_{2.5-0.5x}\text{O}_4$ ($x=0, 0.25, 0.5, 0.75,$ and 1) nanoferrite samples



radii of Mn^{2+} , Li^{1+} and Fe^{3+} are 0.66 \AA , 0.59 \AA , and 0.49 \AA , respectively, in the tetrahedral site and 0.83 \AA , 0.76 \AA , and 0.64 \AA , respectively, in the octahedral site) [31]. The values of the lattice parameter for concentrations $x=0$ and $x=1$ are near previously reported ones prepared by other methods [8, 20, 24]. It is valuable here to note that the lattice parameter increases by 0.016% in this study, while it increases only by 0.004% according to previous studies where Mn replaces Fe only [20]. The reason is that in these studies Mn^{2+} converts to Mn^{3+} during preparation to preserve neutrality of the final composition. The radius of Mn^{3+} (0.645 \AA) is very close to that of Fe^{3+} (0.64 \AA). Furthermore, according to this convergence of the radii, the microstrain is not expected to increase in marked proportions, but a continuous increase of the microstrain values with Mn concentration is noted in our investigated samples (Fig. 3). Such an increase could be due to the replacement of Li^{1+} ions by larger Mn^{2+} ions in our series. This is considered as another clue that Mn^{2+} ions substitute not only Fe^{3+} ions but also Li^{1+} ions. From Fig. 3, it is also clear that the crystallite size decreased on the first addition of Mn^{2+} ($x=0.25$) and then remained almost constant for more additions ($x=0.5$ to 0.75). The crystallite size decreased again at Mn ferrite ($x=1$). A similar behavior was observed by introducing Mn^{2+} ion to Ni and Co ferrites [32, 33]. The crystallite size obtained for $x=0$ ($\text{Li}_{0.5}\text{Fe}_{2.5}\text{O}_4$) agrees well with micro-emulsion and sol-gel preparation techniques [23, 34] but differs from standard ceramic method. The variation of the crystallite size with addition of Mn^{2+} ion could be discussed as follows:

Sol–gel autocombustion reaction consists of a nucleation step followed by particle growth stages in the citrate ion network. The nucleation step occurs through the simultaneous reactions of hydrolysis and condensation. The addition of ammonia solution and raising the temperature enforce the condensation process which in turn increases the nucleation rate in the citrate ion network. In fact, the critical radius of the nucleated particle depends on the individual properties of the metal ions, such as the solubility product K_{SP} of the metal hydroxide $M(OH)_n$ [hydrolysis process] and the pathway to thermodynamically stable metal ferrite [condensation process]. It was reported that, as K_{SP} value increases the crystallite size also increases [35], in this case, the ferric hydroxide ($K_{SP} \approx 10^{-39}$) is common to all ferrite ions. So the size variation can be attributed to K_{SP} values of $M(OH)_n$. For lithium and manganese hydroxides, the solubility products are ($K_{SP} \approx 28$) and ($K_{SP} \approx 10^{-9}$), respectively, so it is expected that the crystallite size decreases with increasing Mn concentration which have been found experimentally. Moreover, Lennard–Jones theory made the conjecture that the unit cell should contract with decreasing of particle size in ionic systems and expand in covalent ones [36]. In this situation, the inverse relation between crystallite size and lattice parameter (Fig. 3) leads to assume that there is a tendency to form covalent bonds in mixed Li–Mn nanoferrites by further addition of Mn^{2+} . This assumption is coherent with the fact that Mn^{2+} and Fe^{3+} ions (3d-half shell) have a tendency to form covalent bonds in tetrahedral sites through sp^3 hybridization [37]. Such a result implies that Mn^{2+} rarely converts to Mn^{3+} in these samples, which again enhances the claim that Mn^{2+} ions substitute not only Fe^{3+} ions but also Li^{1+} ions.

3.2 Physical studies

Porosity values for $Li_{0.5-0.5x}Mn_xFe_{2.5-0.5x}O_4$ series are shown in Fig. 3. It is clear that the total porosity initially decreased then remained fairly constant for $x=0.25, 0.5$, and 0.75 and finally increased at $x=1$. These results could be discussed in the light of the competition between the two types of porosities, inter porosity (P_{inter}) that depends on the crystallite size and intra porosity (P_{intra}) that depends on the ionic radius [38], where

$$P_{tot} = P_{inter} + P_{intra} \quad (5)$$

The drop of porosity of $Li_{0.5-0.5x}Mn_xFe_{2.5-0.5x}O_4$ series by first addition of Mn^{2+} is attributed to the decrease in P_{inter} due to the decrease in crystallite size (about 20 nm). The constancy of P_{tot} for $x=0.25, 0.5$, and 0.75 results from the competition between P_{inter} and P_{intra} . Finally, the increase of P_{tot} at $x=1$ may be attributed to the increase of P_{intra} due to the appreciable increase in the lattice parameter (about

0.07 Å), while P_{inter} plays a less dominant role due to the small decrease in the crystallite size (about 9 nm). Finally, it is noted that the porosity values of these investigated samples are much lower than micro-emulsion method [23] and much greater than ceramic method [24].

3.3 Morphological studies

Figure 4 shows the TEM images for $Li_{0.5-0.5x}Mn_xFe_{2.5-0.5x}O_4$ ($x=0$, i.e., $Li_{0.5}Fe_{2.5}O_4$ and $x=1$, i.e., $MnFe_2O_4$) together with the particle size distribution histograms. The particles are found to be stacked on each other due to their mutual magnetic interactions. Average particle sizes of $Li_{0.5}Fe_{2.5}O_4$ and $MnFe_2O_4$, calculated from TEM, are 50 nm and 30 nm, respectively, which agree well with the XRD crystallite size calculations.

3.4 Infrared spectroscopy analysis

Far infrared spectroscopy is used to study the distribution of the cations in tetrahedral and octahedral sites in ferrites [39]. The IR transmission bands for $Li_{0.5-0.5x}Mn_xFe_{2.5-0.5x}O_4$ series are shown in Fig. 5 and the peak positions are given in Table 1. The bands in the region of $300\text{--}700\text{ cm}^{-1}$ are assigned to the fundamental vibrations of the ferrite crystal lattice. From Fig. 5, it is clear that for $x=0$, ν_2 and ν_3 bands are well separated. However, by addition of Mn^{2+} ion, overlapping occurs between ν_2 and ν_3 with minima in the range of $373\text{--}378\text{ cm}^{-1}$. Furthermore, the minima shift to a lower wavenumber by increasing Mn^{2+} ion content. These results could be accounted for as follows: It is known that ν_2 band, in most ferrites, appears in the range $\approx (390\text{--}490\text{ cm}^{-1})$ and is related to the vibrations of the high valence cations occupying *octahedral site (B site)* such as ($Mn^{3+}\text{--}O$ and $Fe^{3+}\text{--}O$) bonds. Moreover, ν_3 band appears in the range $\approx (310\text{--}360\text{ cm}^{-1})$ and is related to the vibrations of the low valence cations occupying B site such as ($Li^{1+}\text{--}O$, $Mn^{2+}\text{--}O$, and $Fe^{2+}\text{--}O$) bonds [39]. Furthermore, metastable cation distribution occurs due to the nanosize particles [40]. So a lot of cations with different valences occupying B site are found (Mn^{2+} , Fe^{3+} , Mn^{3+} , Fe^{2+} , and Li^{1+}), then the overlap occurs and the metastable cation distribution between A and B sites enhances such overlapping. Moreover, the increased disordering with increasing Mn^{2+} content results in more enhancement of the overlapping [41]. The shift in minima of the overlapped peaks is attributed to the increase in lattice parameter which in turn increases the bond lengths and hence decreases the wavenumber. On the other hand, it was found that the peak of ν_1 (*of tetrahedral site (A site)*) is split to two peaks with increasing Mn^{2+} ion content, which coincides with the fact that Mn^{2+} ions are distributed between A and B sites [36]. Furthermore, it is noticed that ν_4 makes overlapping by introducing Mn^{2+} ion

Fig. 4 TEM images and the particle size distribution histograms for $\text{Li}_{0.5-0.5x}\text{Mn}_x\text{Fe}_{2.5-0.5x}\text{O}_4$ nanoferrite samples. **a** $x=0$ and **b** $x=1$

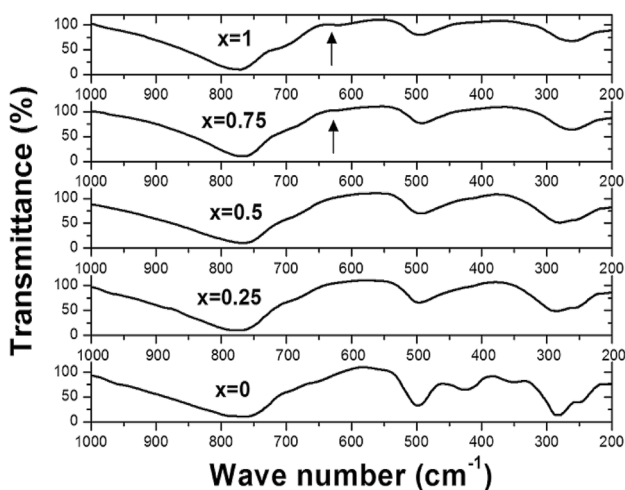
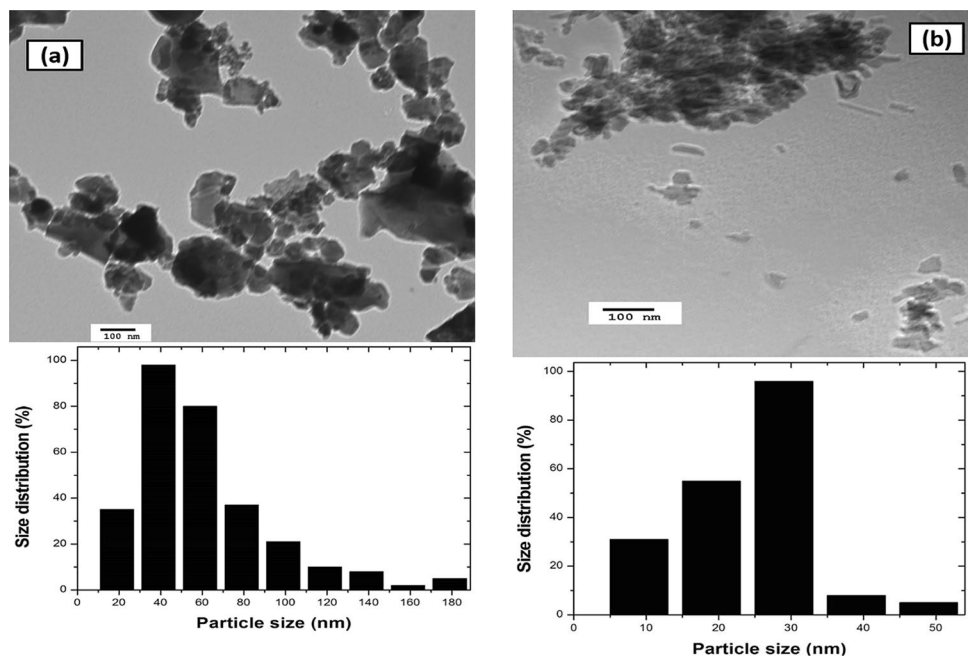


Fig. 5 Infrared transmission spectra for $\text{Li}_{0.5-0.5x}\text{Mn}_x\text{Fe}_{2.5-0.5x}\text{O}_4$ ($x=0, 0.25, 0.5, 0.75,$ and 1) nanoferrite samples

Table 1 Peak positions of the IR transmission spectra of $\text{Li}_{0.5-0.5x}\text{Mn}_x\text{Fe}_{2.5-0.5x}\text{O}_4$ nanoferrite samples

Composition (x)	ν_1 (cm^{-1})	ν_2 (cm^{-1})	ν_3 (cm^{-1})	ν_4 (cm^{-1})
0	583	464	384–336	266–226
0.25	572	Overlapping with minima 378	—	—
0.5	561	376	—	—
0.75	630–553	369	—	—
1	635–554	373	—	—

which is a result of the competition between the overlapping in B site and the splitting in A site, such that the overlapping effect overcomes. Moreover, Fig. 6 represents the variation of ν_1 and ν_2 with Mn concentration and shows that the values of ν_1 and ν_2 generally decrease by addition of Mn. It is found that $(\Delta\nu_1/\Delta x) = 30.8 \text{ cm}^{-1} > (\Delta\nu_2/\Delta x) = 20.4 \text{ cm}^{-1}$, which simply means that the ratio of the Mn content which enters A site is larger than that enters B site. This gives more investigation to the small splitting in the (ν_1) band which could be attributed to the high tendency of Mn^{2+} ions (nearly 80%) to occupy A site. Also Li^{1+} ions have a large tendency to occupy B site if their concentrations do not exceed 0.5 [37, 42].

Over and above, the decreasing of ν_1 and ν_2 by addition of Mn can be discussed as follows. Four parameters may change simultaneously by ion substitution: the total mass of cations, the length and strength of the metal–oxygen bond, and the dimensions of the unit cell. All these parameters affect the position of the IR bands through the well-known relation [43]:

$$\nu \propto \sqrt{\frac{k}{m}}, \quad (6)$$

where k is the force constant.

The decreasing of both (ν_1 and ν_2) comes from the following:

1. The increase in the lattice parameter by increasing Mn content which decreases the bond strength, i.e., force constant k decreases.

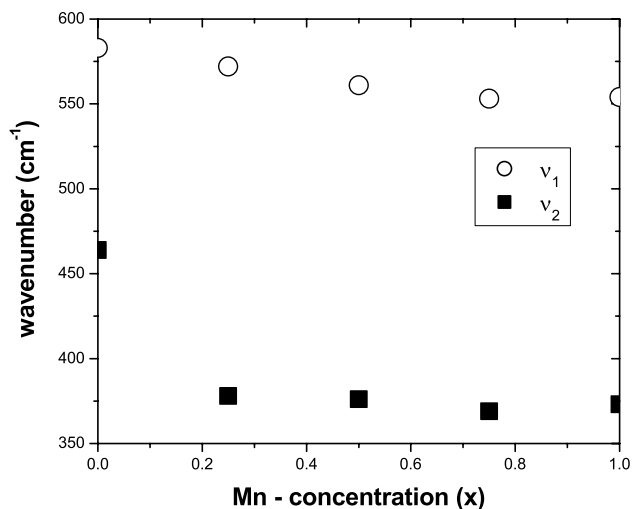


Fig. 6 Variation of wave numbers (ν_1 and ν_2) with Mn concentration (x) for $\text{Li}_{0.5-0.5x}\text{Mn}_x\text{Fe}_{2.5-0.5x}\text{O}_4$ ($x=0, 0.25, 0.5, 0.75$, and 1) nanoferrite samples

- The significant increase in the mass of the compositions by increasing Mn content. Such an increase mainly comes from the substitution of Li^{1+} ion (6.939 g/mol) by Mn^{2+} ion (54.938 g/mol) because Fe^{3+} ion (55.847 g/mol) has nearly the same atomic weight of Mn^{2+} . This may be another proof that Mn^{2+} substitutes both Li^{1+} and Fe^{3+} ions.

According to the previous discussion, the cation distribution can be considered to be $(\text{Mn}_{x-t}\text{Fe}_{1-x+t})_{\text{A site}}[\text{Li}_{0.5-0.5x}\text{Mn}_t\text{Fe}_{1.5+0.5x-t}]_{\text{B site}}\text{O}_4$ which is consistent with previously reported one [24].

3.5 Magnetic studies

The hysteresis curves (M-H) for $\text{Li}_{0.5-0.5x}\text{Mn}_x\text{Fe}_{2.5-0.5x}\text{O}_4$ nanoferrite samples are shown in Fig. 7. The hysteresis parameters (saturation magnetization (M_s), coercivity (H_c), and retentivity (M_r)) were determined from the hysteresis graphs. Moreover, the observed values of the magnetic moments per formula unit in (emu/g) were expressed in Bohr magneton (μ_B), (M_s (experimental) (μ_B)), by substituting the saturation magnetization M_s (emu/g) in Eq. (7) [29] and illustrated in Fig. 8.

$$M_s(\text{experimental})(\mu_B) = \frac{M_s(\text{emu/g}) \times m(\text{g})}{5585}, \quad (7)$$

where m is the molecular mass of the sample. It is clear that the saturation magnetization initially increases till $x=0.5$ then by further increase of Mn^{2+} ion concentration, M_s decreases (but remains larger than its value for $x=0$). This

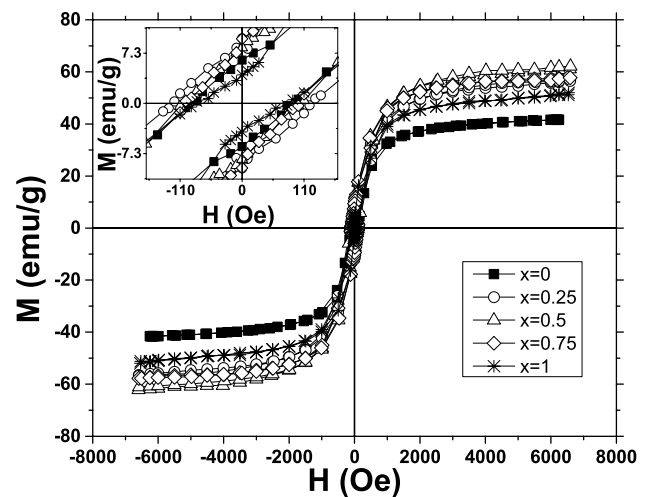


Fig. 7 Hysteresis curves for $\text{Li}_{0.5-0.5x}\text{Mn}_x\text{Fe}_{2.5-0.5x}\text{O}_4$ ($x=0, 0.25, 0.5, 0.75$, and 1) nanoferrite samples. The inset shows the variation of the coercive field (H_c) with the composition (x)

trend is similar to that reported for the microsize samples of $\text{Li}_{0.5-0.5x}\text{Mn}_x\text{Fe}_{2.5-0.5x}\text{O}_4$ [24]. On the contrary, the previous studies for $\text{Li}_{0.5}\text{Mn}_x\text{Fe}_{2.5-x}\text{O}_4$ showed a decrease of M_s with increasing Mn concentration [19, 21, 44]. Again, this proves the entrance of Mn^{2+} on sacrifice of both Li^{1+} and Fe^{3+} . The behavior of M_s in these samples could be discussed according to either the collinear model or the canted model as follows:

- The collinear model:

According to Néel theory and the previous cation distribution, M_s can be calculated by Eq. (8):

$$M_s(\text{calculated}) = (0.5 + 0.5x) \cdot 5\mu_B. \quad (8)$$

Thus, M_s (calculated) shows a linear increase by addition of Mn content, as shown in Fig. 8. Hence, this model does not explain the decrease of M_s for $x > 0.5$.

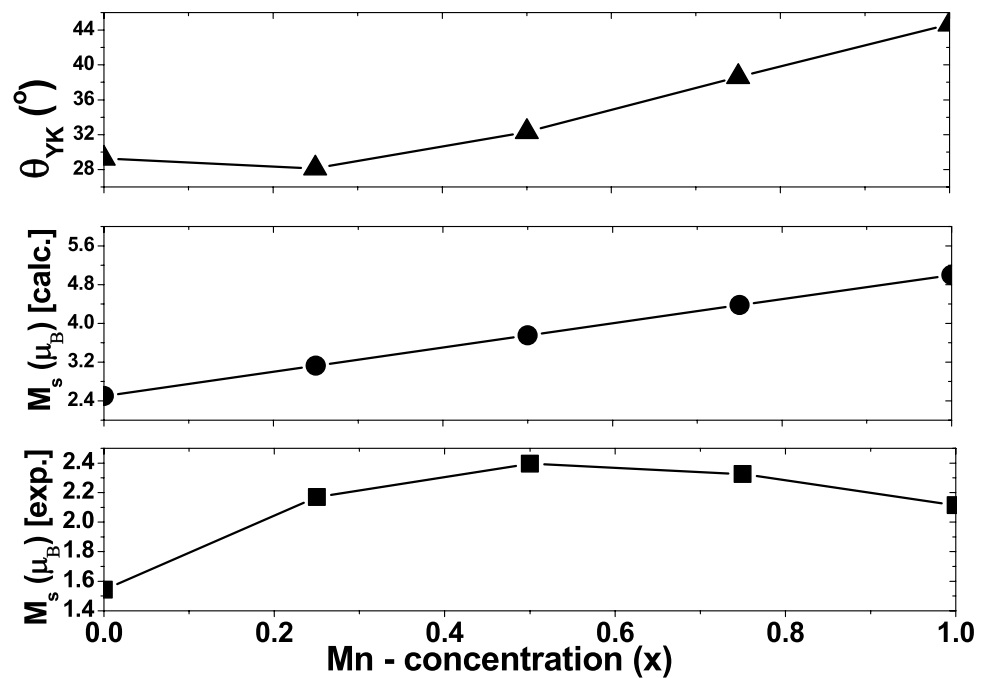
- The canted model:

It is known that increasing the number of magnetic ions in B sites increases the B–B interaction so that it can be comparable to the A–B interaction. At this stage the collinear model fails to apply and the Yafet–Kittel canting angle (θ_{YK}) establishes between the moments in B sites. Thus, the magnetization in this case can be rewritten by Eq. (9) of the canted model:

$$M_s(\text{experimental}) = M_B(\text{calc.}) \cos \theta_{\text{YK}} - M_A(\text{calc.}), \quad (9)$$

where M_A and M_B are the magnetic moments of ions in A and B sites, respectively. The increase of (θ_{YK}) leads the net magnetization to decrease [45, 46]. Accordingly, Mn^{2+}

Fig. 8 The variation of calculated and experimental saturation magnetization (M_s) with Mn concentration for $\text{Li}_{0.5-0.5x}\text{Mn}_x\text{Fe}_{2.5-0.5x}\text{O}_4$ ($x=0, 0.25, 0.5, 0.75, \text{ and } 1$) nanoferrite samples



ion ($5\mu_B$) which has a great tendency to occupy A site will replace Fe^{3+} from A site to B site and increases the number of magnetic moments in B site. Meanwhile, a decrease of Li concentration takes place. This accounts on the decrease of magnetization for high Mn concentration [36, 42, 47].

The coercivity (H_c) and retentivity (M_r) for these investigated samples are graphed with some factors that affect them shown in Fig. 9. The coercivity (H_c) in multidomain structure (≥ 40 nm for other Mn-substituted ferrites [32, 36, 48]) depends on many factors, such as porosity, anisotropy constant (k_1), and crystallite size L . It was reported that H_c is directly proportional to both porosity and anisotropy constant and is inversely proportional to the crystallite size through the relation $H_c = a + (b/L)$, where a and b are constants [29]. It is obvious from Fig. 9 that H_c initially increases at $x=0.25$, then it decreases and remains unaffected till $x=0.75$ (but remains larger than its value for $x=0$) and finally it decreases again at $x=1$. This behavior may be interpreted as follows: k_1 , which results from Fe^{2+} ions, increases with x (according to $\text{Mn}^{2+} + \text{Fe}^{3+} \leftrightarrow \text{Mn}^{3+} + \text{Fe}^{2+}$) [49]. Moreover, the crystallite size decreased from 60 to 42 nm as shown in Fig. 3. Thus, for $x=0.25$, both the crystallite size and k_1 seem to be the dominant factors for increasing (H_c). The decrease of (H_c) up to $x=0.75$ can be explained mainly according to the porosity effect. For $x=1$, it is noted that the crystallite size decreased abruptly (Fig. 9). So, the decrease of (H_c) may be attributed mainly to the transition to stable single-domain structure where the relation $H_c = g - (h/L^{3/2})$

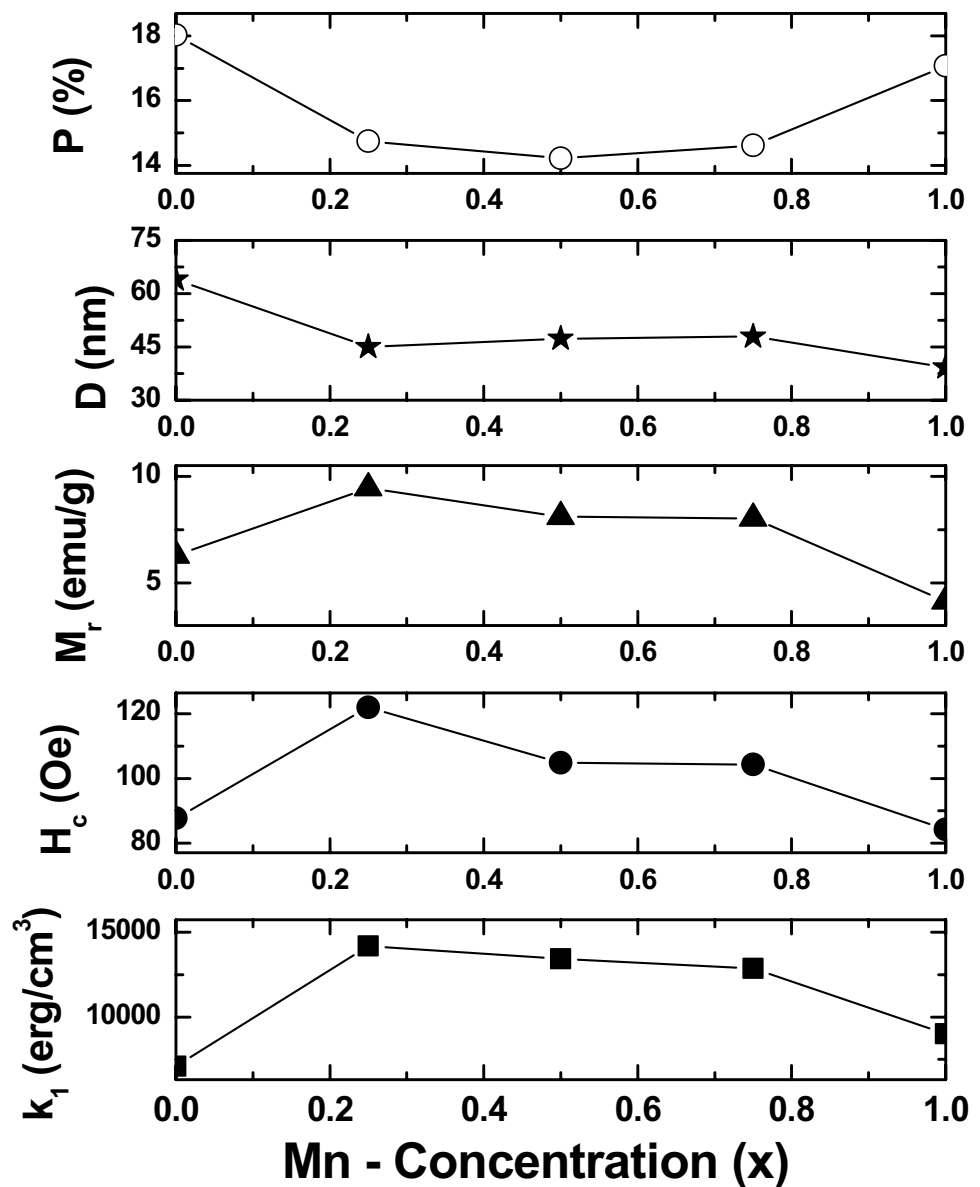
can be used, where g and h are constants [29, 49]. The decrease of the crystallite size leads to a decrease of H_c . Moreover, the decrease of k_1 enhances the decrease of H_c .

Curie temperatures of $\text{Li}_{0.5-0.5x}\text{Mn}_x\text{Fe}_{2.5-0.5x}\text{O}_4$ samples were determined from the initial permeability measurements and are shown in Fig. 10. Obtained values of T_C for $\text{Li}_{0.5}\text{Fe}_{2.5}\text{O}_4$ are comparable to some authors, while the other samples have greater values than different preparation techniques [24, 50]. According to [51, 52], the general factors that affect Curie temperature (T_C) are as follows: the magnitude of the magnetic moments on A and B sites, the distance between the A and B sites, and the exchange integral (J). Obviously, it is seen that the investigated samples show a steep decreasing T_C up to $x=0.75$ followed by a slight increase at $x=1$. Generally, the steep decreasing (which agrees well with [24]) could be attributed to the following:

1. The increase of the lattice parameter by addition of Mn, so the distance between the A and B sites increases and hence the A–B interaction decreases.
2. The decrease of the exchange integral (J) by addition of Mn (where the absolute value of (J) for $\text{Li}_{0.5}\text{Fe}_{2.5}\text{O}_4=29$ K and (J) for $\text{MnFe}_2\text{O}_4=19.1$ K [53]).

On the other hand, the slight increase in T_C at $x=1$ may be attributed to the fact that further addition of Mn leads the magnitude of the total magnetic moments in each A and B sites to increase.

Fig. 9 The porosity (P), crystallite size (D), retentivity (M_r), coercivity (H_c), and anisotropy constant (k_1) for $\text{Li}_{0.5-0.5x}\text{Mn}_x\text{Fe}_{2.5-0.5x}\text{O}_4$ ($x=0, 0.25, 0.5, 0.75, \text{ and } 1$) nanoferrite samples



4 Conclusion

From what the authors got in this study, one can reach the following conclusions: $\text{Li}_{0.5-x}\text{Mn}_x\text{Fe}_{2.5-x}\text{O}_4$ ferrite nanoparticles have been synthesized by the sol-gel autocombustion method. The addition of Mn^{2+} ion to Li ferrite leads the

crystallite size to decrease. The saturation magnetization (M_s) and the coercivity (H_c) are larger for Mn-substituted samples than those for unsubstituted ones. These results introduce a promising magnetic material for many technological applications although Curie temperature decreased by addition of Mn^{2+} ion.

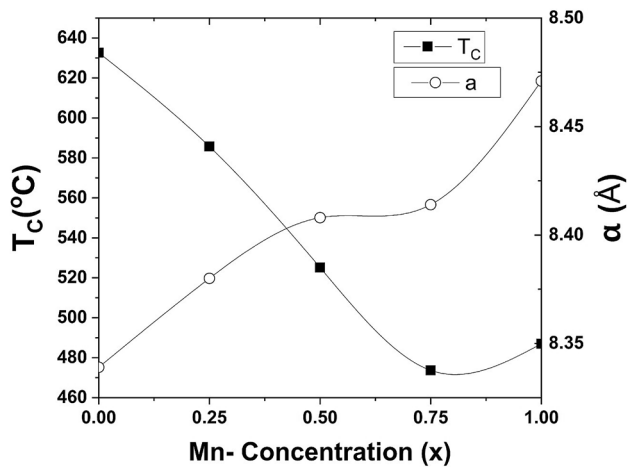


Fig. 10 Variation of Curie temperature (T_c) and lattice parameter (a) with Mn concentration for $\text{Li}_{0.5-0.5x}\text{Mn}_x\text{Fe}_{2.5-0.5x}\text{O}_4$ ($x=0, 0.25, 0.5, 0.75,$ and 1) nanoferrite samples

Acknowledgements The authors express their deep thanks to Prof. Dr. A.A. Sattar and Prof. Dr. A.A. Ghani (Physics Department, Faculty of Science, Ain Shams University) for facilitating the preparation of samples and measurements.

References

- E. Wolska, K. Stempin, O.K. Hobbs, *Solid State Ionics* **101**, 527 (1997)
- M.N. Obrovac, O. Mao, J.R. Dahn, *Solid State Ionics* **112**, 9 (1998)
- Y. Sakurai, H. Arai, J. Yamaki, *Solid State Ionics* **113**, 29 (1998)
- J.R. Dahn, U. Vomsacken, C.A. Micha, *Solid State Ionics* **44**, 87 (1990)
- Y.S. Cho, Y.L. Burdick, V.R.W. Amarakoon, *J. Am. Ceram. Soc.* **82**, 1416 (1999)
- P.S.A. Kumar, J.J. Shrotri, S.D. Kulkarni, C.E. Deshpande, S.K. Date, *Mater. Lett.* **27**, 293 (1996)
- P.D. Baba, G.M. Argentina, *Microw. Theory Technol.* **22**, 654 (1974)
- D. Madhavaprasad, G. Ganapathi Rao, H.R. Daruvuru, C. Arun Kumar, K. Samatha, S. Bharadwaj, *Process Appl. Ceram.* **11**(1), 7 (2017)
- I.Z. Rahman, T.T. Ahmed, *J. Magn. Magn. Mater.* **290–291**, 1576 (2005)
- P. Sainamthip, V.R.W. Amarakoon, *J. Am. Ceram. Soc.* **71**(2), C92 (1988)
- S. Komarneni, E. Fregeau, E. Breval, R. Roy, *J. Am. Ceram. Soc.* **71**(1), C26 (1988)
- S. Malathi, P. Seenuvasakumaran, *Int. J. Phys. Math. Sci.* **10**(8), 409 (2016)
- A.R. Bueno, M.L. Gregori, M.C.S. Nobrega, *Mater. Chem. Phys.* **105**, 229 (2007)
- A. Verma, R. Chatterjee, *J. Magn. Magn. Mater.* **306**, 313 (2006)
- Fu Yen-Pei, C.-S. Hsu, *Solid State Commun.* **134**(3), 201 (2005)
- X. Qi, Ji Zhou, Z. Yue, Z. Gui, L. Li, *Mater. Sci. Eng. B* **99**, 278 (2003)
- Fu Yen-Pei, S. Tsao, Hu Chen-Ti, Y.-D. Yao, *J. Alloys Compds* **395**, 272 (2005)
- P.P. Hankare, R.P. Patil, U.B. Sankpal, S.D. Jadhav, I.S. Mulla, K.M. Jadhav, B.K. Chougule, *J. Magn. Magn. Mater.* **321**, 3270 (2009)
- Y.P. Fu, C.S. Hsu, *J. Alloys Compds.* **391**(1–2), 185 (2005)
- R.P. Patil, B.V. Jadhav, P.P. Hankare, *Results Phys.* **3**, 214 (2013)
- B. Ramesh, M. Lakshmiopathi Rao, *J. Alloys Compds* **551**, 527 (2013)
- I. Soibam, S. Phanjobam, *Indian J. Phys.* **87**(2), 121 (2013)
- M. Sharif, J. Jacob, M. Javed, A. Manzoor, K. Mahmood, M.A. Khan, *Phys. B: Condens. Matter* **567**, 45 (2019)
- S.A. Mazen, N.I. Abu-Elsaad, *J. Magn. Magn. Mater.* **324**, 3366 (2012)
- H. Waqas, A.H. Qureshi, *J. Therm. Anal. Calorim.* **100**, 529 (2010)
- B.D. Cullity, S.R. Stock, *Elements of X-ray diffraction* (Prentice-Hall Inc., 3rd edition, 2001).
- G.K. Williamson, W.H. Hall, *Acta Metall.* **1**, 22 (1953)
- V.D. Mote, Y. Purushotham, B.N. Dole, *J. Theor. Appl. Phys.* **6**, 1 (2012)
- B.D. Cullity, C.D. Graham, *Introduction to magnetic materials* (Wiley, Hoboken, New Jersey, 2nd edition, 2009)
- A.A. Sattar, W.R. Agami, *J. Alloys Compds.* **496**, 341 (2010)
- R.D. Shannon, *Acta Crystallogr. A* **32**, 751 (1976)
- M.K. Shobana, S. Sankar, *J. Magn. Magn. Mater.* **321**(14), 2125 (2009)
- M.K. Shobana, S. Sankar, *J. Magn. Magn. Mater.* **321**(6), 599 (2009)
- R. Cheruku, G. Govindaraj, L. Vijayan, *Mater. Res. Express* **4**, 12 (2017)
- G. Gnanaprakash, J. Philip, B. Raj, *Mater. Lett.* **61**, 4545 (2007)
- R. Iyer, R. Desai, R.V. Upadhyay, *Bull. Mater. Sci.* **32**, 141 (2009)
- E.W. Gorter, *Philips Res. Rept.* **9**, 295 (1954)
- W.D. Kigery, H.K. Bowen, D.R. Uhlmann, *Introduction of ceramics* (Wiley, New York, London, 1996)
- K. Mohan, Y.C. Venudhar, *J. Mat. Sci. Lett.* **18**, 13 (1999)
- B. Ramesh, D. Ravinder, *Mater. Lett.* **62**, 2043 (2008)
- E. Wolska, P. Piszora, W. Nowicki, J. Darul, *Int. J. Inorg. Mater.* **3**, 503 (2001)
- C. Wende, Kh Olimov, H. Modrow, F.E. Wagner, H. Langbein, *Mater. Res. Bull.* **41**, 1530 (2006)
- A.D. Cross, R.A. Jones, *Introduction to Practical Infrared Spectroscopy* (Butterworths, London, 3rd edition 1969).
- Z.K. Heiba, M.B. Mohamed, *Appl. Phys. A* **124**, 818 (2018)
- C. Kittel, *Phys. Rev.* **73**, 810 (1948)
- S.S. Suryawanshi, V. Deshp, S.R. Sawant, *J. Mater. Chem. Phys.* **59**, 199 (1999)
- P.P. Hankare, R.P. Patil, U.B. Sankpal, S.D. Jadhav, P.D. Lokhande, K.M. Jadhav, R. Sasikala, *J. Solid State Chem.* **182**, 3217 (2009)
- C.F. Zhang, X.C. Zhong, H.Y. Yu, Z.W. Liu, D.C. Zeng, *Phys. B* **404**(16), 2327 (2009)
- M.A. Ahmed, *J. Magn. Magn. Mater.* **322**, 763 (2010)
- N. Vasudevan Nair, S. Resmi, *IOSR. J. Appl. Phys.* **11**(2), 54 (2019)
- M. Zheng, X.C. Wu, B.S. Zou, Y.J. Wang, *J. Magn. Magn. Mater.* **183**, 152 (1998)
- C. Rath, S. Anand, R.P. Das, K.K. Sahu, S.D. Kulkarni, S.K. Date, N.C. Mishara, *J. App. Phys.* **91**(4), 2211 (2002)
- C.M. Srivastava, G. Srinivasan, N.G. Nanadikar, *Phys. Rev. B* **19**, 499 (1979)

Publisher's Note Springer Nature remains neutral with regard to jurisdictional claims in published maps and institutional affiliations.